

p21 induces a senescence program and skeletal muscle dysfunction



Davis A. Englund^{1,2}, Alyssa Jolliffe^{1,2}, Zaira Aversa^{1,2}, Xu Zhang^{1,2}, Ines Sturmlechner^{3,4}, Ayumi E. Sakamoto^{1,2}, Julianna D. Zeidler^{1,5}, Gina M. Warner^{1,5}, Colton McNinch⁶, Thomas A. White^{1,2}, Eduardo N. Chini^{1,5,7}, Darren J. Baker^{1,3,7,8}, Jan M. van Deursen^{3,8}, Nathan K. LeBrasseur^{1,2,7,9,*}

ABSTRACT

Recent work has established associations between elevated p21, the accumulation of senescent cells, and skeletal muscle dysfunction in mice and humans. Using a mouse model of p21 overexpression (p21OE), we examined if p21 mechanistically contributes to cellular senescence and pathological features in skeletal muscle. We show that p21 induces several core properties of cellular senescence in skeletal muscle, including an altered transcriptome, DNA damage, mitochondrial dysfunction, and the senescence-associated secretory phenotype (SASP). Furthermore, p21OE mice exhibit manifestations of skeletal muscle pathology, such as atrophy, fibrosis, and impaired physical function when compared to age-matched controls. These findings suggest p21 alone is sufficient to drive a cellular senescence program and reveal a novel source of skeletal muscle loss and dysfunction.

© 2022 The Author(s). Published by Elsevier GmbH. This is an open access article under the CC BY-NC-ND license (<http://creativecommons.org/licenses/by-nc-nd/4.0/>).

Keywords Cellular senescence; DNA damage; Senescence-associated secretory phenotype; Aging; Sarcopenia; Physical function; Fibrosis

1. INTRODUCTION

Cellular senescence is a cell fate initiated by diverse forms of molecular and cellular damage or dysfunction. While cellular senescence plays important physiological roles, it is clear that the accumulation of senescent cells is a driver of degenerative phenotypes, disabilities, and diseases [1–4]. Core features of senescent cells include a persistent DNA damage response, activation of cell-cycle regulators and anti-apoptotic pathways, increased inflammatory signaling, and the senescence-associated secretory phenotype (SASP), a heterogeneous collection of hundreds of secreted factors enriched in cytokines, chemokines, matrix remodeling proteins, and growth factors. The SASP is a particularly detrimental feature of cellular senescence, as it can reinforce the senescence program and transmit senescence to otherwise healthy cells, locally and systemically [5,6].

Recent work from our group shows skeletal muscle is susceptible to certain cellular stressors, such as inflammation and DNA damage, and to the induction of the senescence program. Interestingly, elevated levels of the cyclin-dependent kinase inhibitor p21 was a distinguishing feature of skeletal muscle from old mice and humans [7]. Moreover, we uncovered an inverse association between levels of p21 in skeletal muscle and measures of strength and function, that was conserved across species [7]. These data suggest that p21 may act as a mediator of the senescence program in skeletal muscle. While intriguing, studies that enable the manipulation of p21 are required in order to assess the

extent to which p21 directly contributes to the creation of pathology-causing senescent cells and skeletal muscle dysfunction.

Here, we exploit a mouse model that allows for the overexpression of p21 (p21OE) and examine molecular features of cellular senescence, histological parameters of skeletal muscle pathology, and clinically-relevant measures of skeletal muscle function. We find that p21 alone induces a deleterious phenotype in skeletal muscle that includes key features of the cellular senescence program. These data suggest that targeting senescent cells may benefit muscle health and function.

2. MATERIAL AND METHODS

2.1. Experimental model

Hprt-Cre mice were purchased from The Jackson Laboratory (#004302) and crossed onto C57BL6 for at least 10 generations. *Ai14* mice (*Rosa26-LoxP-STOP-LoxP-tdTomato*) and *LSL-p21* mice (*Col1a1-LoxP-STOP-LoxP-p21*) were described previously [16,33]. Female *Hprt-Cre*+/+ mice were crossed with *LSL-p21*+/+; *Ai14*/*Ai14* males to generate *LSL-p21*+/+ *Ai14*+/+ mice (p21OE) and *Ai14*+/+ littermates (control). In both p21OE and control mice, the *LoxP-STOP-LoxP* (LSL) cassettes in front of the *p21* transgene and *tdTomato* transgene are recombined by *Hprt-Cre* in the oocyte. All resultant experimental mice did not express *Hprt-Cre* themselves. Both male and female mice were used in experiments at 2–3 months of age. Experimental procedures involving laboratory mice were reviewed and

¹Robert and Arlene Kogod Center on Aging, Mayo Clinic, Rochester, MN, USA ²Department of Physical Medicine and Rehabilitation, Mayo Clinic, Rochester, MN, USA ³Department of Pediatric and Adolescent Medicine, Mayo Clinic, Rochester, MN, USA ⁴Department of Pediatrics, Molecular Genetics Section, University of Groningen, University Medical Center Groningen, Groningen, Netherlands ⁵Department of Anesthesiology and Perioperative Medicine, Mayo Clinic, Jacksonville, FL, USA ⁶Division of Biomedical Statistics and Informatics, Mayo Clinic, Rochester, MN, USA ⁷Paul F. Glenn Center for the Biology of Aging at Mayo Clinic, Rochester, MN, USA ⁸Department of Biochemistry and Molecular Biology, Mayo Clinic, Rochester, MN, USA ⁹Department of Physiology and Biomedical Engineering, Mayo Clinic, Rochester, MN, USA

*Corresponding author. Robert and Arlene Kogod Center on Aging, Mayo Clinic, Rochester, MN, USA. E-mail: LeBrasseur.Nathan@mayo.edu (N.K. LeBrasseur).

Received November 17, 2022 • Revision received November 28, 2022 • Accepted December 1, 2022 • Available online 9 December 2022

approved by the Institutional Animal Care and Use Committee of the Mayo Clinic.

2.2. Tissue processing

Immediately following euthanasia, skeletal muscles were excised and weighed, then pinned to a cork block at resting length, covered with Tissue Tek Optimal Cutting Temperature (OCT) compound (Sakura Finetek, Torrance, CA, USA), and quickly frozen in liquid nitrogen-cooled isopentane and stored at -80°C for histochemical analysis. Additional skeletal muscles and organs were collected and flash frozen in cryotubes and stored at -80°C for RNA and protein extraction. Blood was collected with a 27G $\times \frac{1}{2}$ " Monoject needle (Covidien, Dublin, Ireland) via the vena cava. After blood was collected, it was stored on ice and spun down in a centrifuge. The top layer of plasma was removed and stored at -80°C for future analysis.

2.3. Histochemistry

Frozen soleus and plantaris muscles in OCT from female ($n = 2-3$ /group) and male ($n = 2-3$ /group) mice were sectioned using a Leica CM3050 S Cryostat (Leica Biosystems, Deer Park, IL, USA) at a thickness of $7\ \mu\text{m}$ and at -23°C . Sections were air dried at room temperature for 1 h and stored at -20°C . To determine total fiber number, fiber type distribution, cross-sectional area, and nuclear number, soleus and plantaris cross sections were incubated in a cocktail of isotype-specific antibodies for MyHC1 anti-Ms IgG2B (1:100, BA.D5) and MyCH2A anti-Ms IgG1 (1:100, SC.71) from Developmental Studies Hybridoma Bank (Iowa City, IA, USA), and anti-dystrophin anti-Rb IgG (1:100, Abcam, St. Louis, MO, USA) for 1 h. Sections were washed with PBS and incubated in the secondary antibodies Alexa Fluor 647 Gt anti-Ms IgG2B (1:200), Alexa Fluor 555 Gt anti-Ms IgG1 (1:200), and Alexa Fluor 488 Gt anti-Ms IgG1 (1:200), from Invitrogen (Carlsbad, CA, USA) for 90 min. SlowFade Gold antifade mountant with DAPI (Invitrogen) was used for DAPI staining and coverslipping. To visualize nuclei with DNA damage, soleus cross sections were thawed at room temperature for 5 min, fixed in 4% PFA in PBS for 10 min, washed with PBS and permeabilized with 0.1% Triton X-100 diluted in PBS for 5 min. Sections were then blocked with 1% BSA in PBS at room temperature for 1 h and incubated overnight at 4°C with anti-dystrophin (mouse IgG2B, 1:100; Abcam) and anti- γH2AX (Rabbit IgG, 1:300; Cell Signaling Technology, Inc. Danvers, MA, USA) antibodies. The next day, sections were washed with PBS and incubated at room temperature in secondary antibodies Alexa Fluor 647 Gt anti-Ms IgG2B (1:200) and Alexa Fluor 488 Gt anti-Ms IgG (1:200) for 75 min and washed again. SlowFade Gold antifade mountant with DAPI (Invitrogen) was used for DAPI staining and coverslipping. To quantify fibrosis, soleus cross sections were stained with picosirius red (PSR) for 1 h (Polysciences, Warrington, PA, USA) and rinsed in acetic acid, according to the manufacturer's instructions.

2.4. Microscopy and image quantification

Images were acquired with a Zeiss (Oberkochen, Germany) Axio Imager microscope at $20\times$ magnification and tiled using Zen software to capture whole-muscle cross sections. Fiber number, fiber type distribution, and cross-sectional area were quantified on whole-muscle cross sections with Myovision analysis software [34]. γH2AX -positive nuclei were quantified from representative regions of interest (ROIs) using Myovision analysis software. PSR stained cross sections were imaged under both bright-field and polarized light conditions. Images were analyzed using ImageJ software as described previously [35].

2.5. RNA isolation and RT-qPCR

RNA was isolated from whole tissue homogenates from female ($n = 2-5$ /group) and male ($n = 2-5$ /group) mice using Trizol Reagent (Invitrogen, Austin, TX, USA) following the manufacturer's protocol. RNA was then quantified with a NanoDrop 8000 spectrophotometer (ThermoFisher, Waltham, MA, USA). cDNA was synthesized from 1,000 ng of total RNA using M-MLV reverse transcriptase (Invitrogen) and real-time PCR was performed with PerfeCTa FastMix II Low ROX (QuantaBio) and the QuantStudio 5 Real-Time PCR system (ThermoFisher). Gene expression was analyzed by the $\Delta\Delta\text{CT}$ method and normalized to the reference gene TBP. Primers and probes are listed in the supplementary information.

2.6. RNA-sequencing

Library preparation and sequencing was performed at the Mayo Clinic Medical Genomics Facility (Mayo Clinic, Rochester, Minnesota). Total RNA concentration and quality were determined using a Qubit fluorometer (Invitrogen). cDNA libraries were prepared with 200 ng of total RNA using TruSeq Stranded mRNA Sample Prep Kit (Illumina, #20020595) according to the manufacturer's instructions. The concentration and size distribution of the completed libraries were determined using an Agilent TapeStation D1000 and Qubit fluorometry. Libraries were sequenced following the standard protocol for the Illumina NovaSeq™ 6000 (Illumina, #20040719) and using the NovaSeq XP 2-Lane kit (Illumina, #20043130) for individual lane loading. Fastq files of pair-end RNA-seq reads were aligned with STAR 2.7.0 to the reference genome with default parameters. Gene level counts were obtained using FeatureCounts from the SubRead package. Expression analysis was performed using R package DESeq2 1.10.1. Gene set enrichment analysis (GSEA) was performed using software GSEA (v.4.0.3) [36]. The GeneMANIA application within Cytoscape was used for network category analysis and data visualization [37]. The color of the node for each gene is scaled to an interaction score, defined as the effect of a given gene on the selected pathway. Edges represent network categories. Network categories include: coexpression, genes are linked if their expression levels are similar across conditions in a gene expression study; colocalization, genes are linked if they are both expressed in the same tissue or if their gene products are both identified in the same cellular location; coexpression, genes are functionally associated if the effects of perturbing one gene were found to be modified by perturbations to a second gene; shared protein domains, genes are linked based on their protein domain similarity; physical interaction, genes are linked if they were found to interact in a protein-protein interaction study.

2.7. Western blot

Total protein extracts from female ($n = 4-5$ /group) and male ($n = 2-3$ /group) mice were prepared from flash frozen quadriceps tissue in cell lysis buffer (Cell Signaling Technology) with protease inhibitor cocktail (Sigma) and phenylmethylsulfonyl fluoride. Protein concentration was determined using the DC Protein Assay (Bio-Rad). Equal amounts of protein ($30\ \mu\text{g}$) were resolved by SDS-PAGE and transferred to a PVDF membrane (Bio-Rad). The membrane was blocked with 5% nonfat dry milk and then incubated overnight at 4°C with a rabbit monoclonal anti-p21 antibody (ab188224, Abcam). A rabbit monoclonal anti-GAPDH antibody (#5174, Cell Signaling Technology) was used as loading control. Following primary antibody incubation, the membrane was washed in TBST, incubated 1 h at room temperature with a mouse anti-rabbit IgG-HRP secondary antibody (sc-2357, Santa Cruz Biotechnology) and washed again in TBST. Signal was

developed using SuperSignal West Femto Maximum Sensitivity Substrate (Thermo Fisher Scientific).

2.8. Circulating senescence factors

To quantify the concentrations of senescence-related proteins, blood plasma from female ($n = 2-6$ /group) and male ($n = 2-6$ /group) mice was analyzed using commercially available multiplex magnetic bead-based immunoassays (R&D Systems) on the Luminex xMAP multi-analyte profiling platform and analyzed on MAGPIX System (Merck Millipore). All assays were performed according to the manufacturer's protocols. The biomarkers quantified with this method include: GDF15, MMP2, MMP3, OPN, PAI1, and TNFR1. Proteins that did not reach reliable detection levels on the Luminex platform were run on ProteinSimple Ella assay (Bio-Techne, San Jose, CA, USA), in a subset of samples that had adequate volumes of remaining plasma. The biomarkers quantified with this method include TNF-alpha, IL6, and CCL2. All reported protein concentrations had over 80% detectability across samples.

2.9. Muscle fiber isolation and mitochondrial respiration

Immediately after excision, approximately 5 mg of quadriceps from female ($n = 3-4$ /group) and male ($n = 3-4$ /group) mice was placed in BIOPS buffer to analyze mitochondrial respiration and ROS production. The muscle fibers were gently teased apart manually using blunt scalpels and permeabilized in 2 mL BIOPS buffer with 50 μ g/mL saponin on ice for 20 min. Samples were washed in MiR05 buffer for 10 min and placed in an Oxygraph-2k (Oroboros Instruments, Innsbruck, Austria) for analysis. Measurements were performed in MiR05 containing 25 μ M blebbistatin to block contractile activity. Medical-grade oxygen was added to each chamber containing muscle samples until achieving 400 μ M oxygen concentration, followed by sequential additions of 2 mM malate, 5 mM pyruvate, 5 mM glutamate, 5 mM succinate (state 2), 1 mM ADP (state 3), FCCP (carbonyl cyanide 4-(trifluoromethoxy) phenylhydrazone, an oxidative phosphorylation uncoupler) titration up to 1 μ M (or until oxygen flux no longer increases) to achieve maximal respiration (Max), 0.5 μ M rotenone, and 2.5 μ M antimycin A. After each addition, the O_2 flux signal was given time to stabilize before adding the next reagent. Data were recorded and analyzed using DatLab 5 software. ETS (electron transport system)-dependent oxygen consumption rate per wet mg of tissue was determined by subtracting residual respiration (oxygen consumption rate after antimycin A addition). For maximal respiration associated with complex I (Max CI), respiratory rates after FCCP titration were subtracted from rotenone-independent rates, and the remaining flux (subtracted from residual respiration) was considered complex II-dependent maximal respiration (Max CII). Coupled respiration was calculated by subtracting state 3 from state 2. Spare capacity is the difference between maximal respiration and state 3.

2.10. Phenotyping

Phenotypic tests were performed on female ($n = 4-6$ /group) and male ($n = 4-6$ /group) mice within two weeks prior to necropsy. Body composition, including total body fat and lean mass, was determined with an EchoMRI-100 (Houston, TX, USA), as described previously [38]. Exercise capacity, defined as work to exhaustion on a motorized treadmill (Columbus Instruments, Columbus, OH, USA) and forelimb grip strength (Columbus Instruments) were performed as previously described [39].

2.11. Statistical analysis

Results are presented as mean \pm SD. Data were analyzed with GraphPad Prism software via unpaired two-tailed Student's *t*-test. Significance was set at a $P < 0.05$. For correlation analysis, a two-

tailed Spearman correlation was used. An FDR cutoff of 0.25 was applied to GSEA.

3. RESULTS

3.1. p21OE mice demonstrate transgene coexpression across tissues

To study the direct effects of p21, we established a transgenic mouse model that allows for Cre-inducible coexpression of the fluorescent reporter tdTomato and p21 (Figure 1A). To validate this model, we used primers designed to capture expression levels of the transgene *tdTomato* and exogenous (transgene) and endogenous expression of *p21* together (total p21). We assessed *tdTomato* and total *p21* in skeletal muscle (quadriceps), heart, liver, and kidney samples from p21OE (*LSL-p21/+;Ai14/+*) and control (*Ai14/+*) mice. Consistent with effective recombination, p21OE and control mice both display expression of *tdTomato* (Figure 1B). p21OE mice alone exhibit robust increases in total *p21*, demonstrating effective transgene activation and validating our experimental and control models (Figure 1C). p21OE mice were viable and born at Mendelian ratios.

3.2. p21 is sufficient to activate a senescence program in skeletal muscle

To determine if p21 influences known inducers and reinforcers of the senescence program, we looked at expression levels of cell-cycle regulators, including endogenous *p21*, *E2f2*, and *Zmat3*, anti-apoptotic Bcl-2 family members *Bcl2* and *Bcl2l1*, and markers of genotoxic stress and DNA damage *Igfbp3*, *Igfbp7*, *Gadd45a*, *Atm*, *Atf4*, and *Tgfb1* (Figure 2A), and found these markers to be consistently upregulated in p21OE mice. Additionally, inflammatory markers and components of the cGAS-STING and NF- κ B pathways (critical regulators of inflammatory status and the SASP in senescent cells), including *Sting1*, *Irf7*, *Tnfrsf1b*, *Cxcl9*, *Mmp2*, *Mmp3*, *Icam1*, *Serpine2*, and *Il18* were elevated in skeletal muscle of p21OE mice (Figure 2B). Levels of *p16^{INK4a}* expression were not altered by p21 in skeletal muscle (Fig. S1). To further establish the effects of p21 on the skeletal muscle transcriptome, we performed RNA-seq and gene set enrichment analysis (GSEA) comparing p21OE mice to control mice. Curated pathways specific to cellular senescence were significantly enriched in p21OE mice (e.g., SenMayo, SASP, and NF- κ B pathways (Figure 3A)) and several KEGG pathways indicative of the senescence program were also enriched in p21OE mice (e.g., p53 signaling, cytokine to cytokine interaction, and cytosolic DNA sensing pathway (Figure 3B [8,9])).

3.3. p21 leads to a senescent profile across skeletal muscles

Following the discovery of a transcriptional signature for cellular senescence in the quadriceps of p21OE mice, we aimed to more extensively phenotype skeletal muscle in a larger cohort. First, protein levels of p21 were assessed in skeletal muscle which revealed robust accrual in samples from p21OE mice (Figure 4A). This was followed by the examination of senescence markers in skeletal muscles with unique anatomical and physiological properties (soleus and diaphragm), together with the quadriceps. The upregulation of key senescence inducers and inflammatory components was conserved across distinct skeletal muscles of p21OE mice (Figure 4B).

3.4. p21 drives mitochondrial dysfunction, DNA damage, and the SASP

Next, we aimed to examine the physiological consequences of a molecular profile consistent with cellular senescence. Mitochondrial dysfunction is a hallmark of cellular senescence, and *in vitro* p21 has

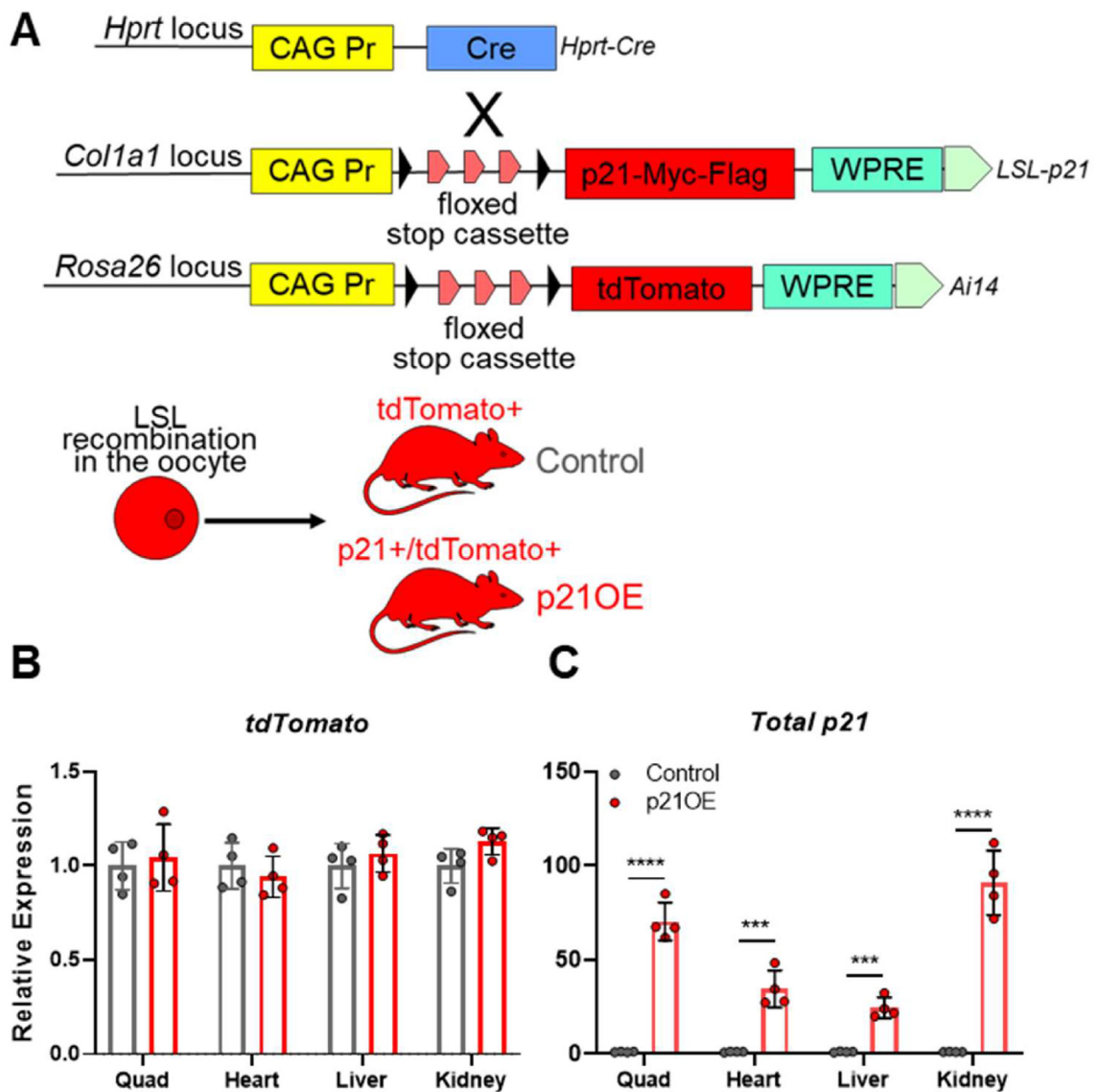


Figure 1: Engineering of a Cre/Lox mouse that allows for ubiquitous coexpression of p21 and tdTomato. (A) Schematic representation of transgenes used for Cre expression (*Hprt-Cre*) and Cre-inducible expression of p21 (*LSL-p21* for *LoxP/STOP/LoxP-p21*) and tdTomato (*Ai14*). (B–C) tdTomato and p21 expression across tissues assessed by RT-qPCR ($n = 4/\text{group}$). Data represent means \pm SD. *** $P < 0.001$, **** $P < 0.0001$, as assessed by unpaired two-tailed t tests.

been shown to directly impact mitochondrial function [10,11]. Thus, we isolated muscle fibers from the quadriceps and utilized high-resolution respirometry to measure mitochondrial oxygen consumption in permeabilized fibers. Muscle fibers of p21OE mice exhibited a general decline in mitochondrial function and marked reductions in spare capacity, maximal (Max) oxygen consumption rate (OCR), and the contribution of complex I (Max C) to Max (Figure 5A) [12]. DNA damage plays a causal role in aging and is recognized as a lynchpin of the senescence program [13,14]. Interestingly, p21 has been shown to cause DNA damage *in vitro* [10]. Utilizing antibody- and microscopy-based techniques to identify γ H2AX-containing DNA damage foci in skeletal muscle (Figure 5B), we confirmed a strong signal for DNA damage in myonuclei (nuclei specific to muscle fibers) and in the nuclei of mononuclear cells that reside in the interstitial microenvironment in p21OE mice (Figures 5C).

Additionally, p21, mitochondrial dysfunction, and DNA damage have all been implicated as key players in the development of a pro-

inflammatory secretory phenotype (the SASP), characteristic of senescent cells [15,16]. We utilized multiplex-based platforms to assay circulating SASP factors in blood plasma. p21OE mice demonstrate substantive increases in a collection of biologically diverse SASP-related proteins, including GDF15, MMP2, MMP3, OPN, PAI1, TNFR1, TNF-alpha, IL6, and CCL2, most of which, in humans, we have demonstrated increase with chronological age and clinical indices of biological age (Figure 5D). Additional proteins with detectable levels can be found in the supplementary information. The generation of a robust SASP is consistent with the recent observation that p21, when elevated, induces an immediate secretory phenotype, referred to as the p21-associated secretory phenotype or PASP, which becomes an integral part of the SASP once damaged or stressed cells enter a senescent state [16].

3.5. p21 induces pathological features in skeletal muscle

Lastly, we wanted to determine the extent to which p21 drives signs of skeletal muscle pathology, including atrophy, alterations in muscle

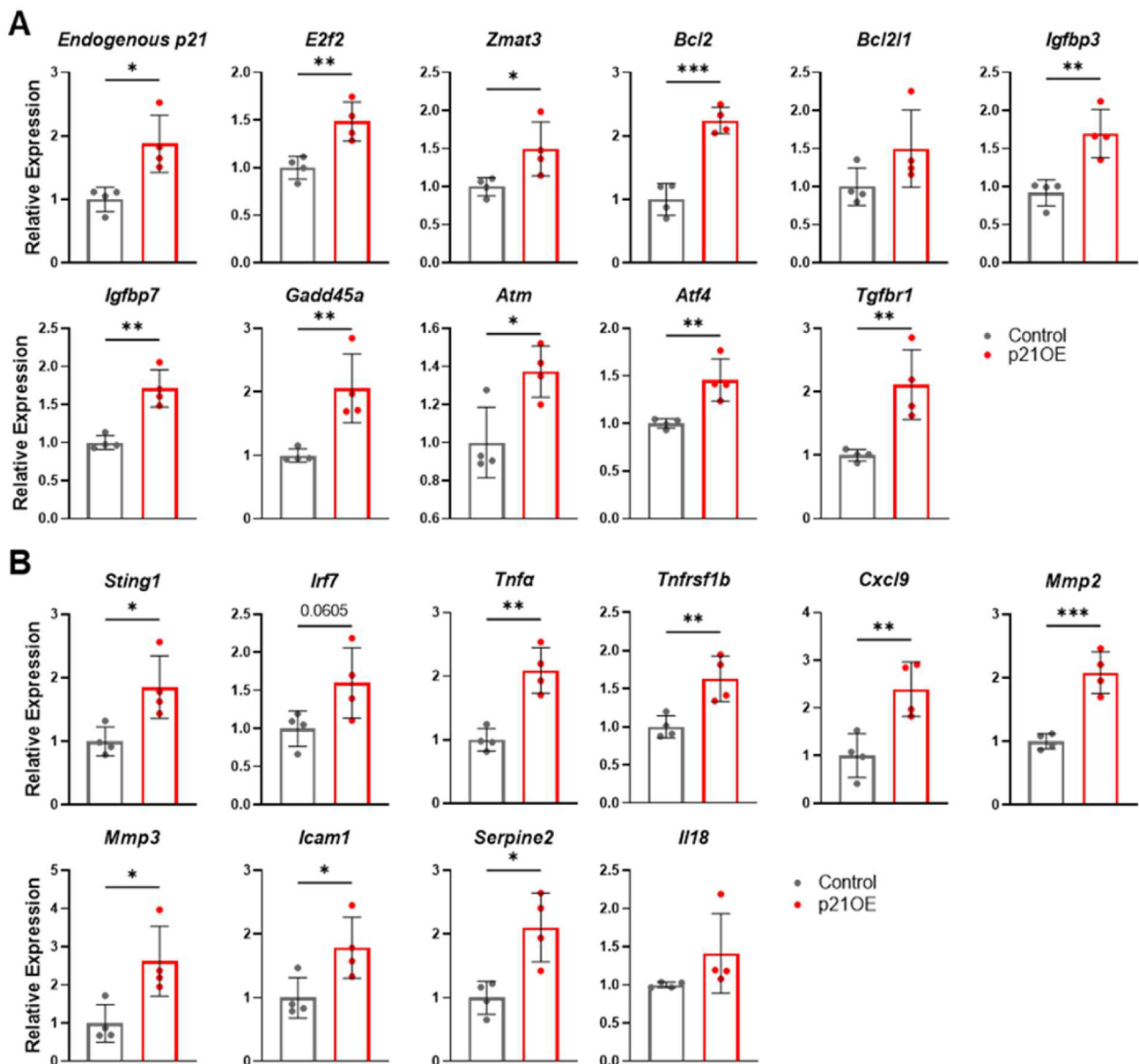


Figure 2: p21 increases expression of inducers and reinforcers of the senescence program in skeletal muscle. (A) Cell-cycle regulators and markers of DNA damage and (B) Inflammatory regulatory factors assessed in the quadriceps by RT-qPCR (n = 4/group). Data represent means \pm SD. * $P < 0.05$; ** $P < 0.01$; *** $P < 0.001$, as assessed by unpaired two-tailed *t* tests.

fiber composition, fibrosis, and reductions in physical function, which are prominent features of certain congenital and chronic diseases, injury, inactivity, and advanced age. First, we examined body composition, bone length, and skeletal muscle weights (quadriceps, soleus, and plantaris) and found overt signs of reduced whole-body lean mass and skeletal muscle weights in p21OE mice, in the absence of differences in bone length (Figure 6A). Consistent bone length between groups indicates p21OE mice did not experience overt developmental deficits.

Next, we utilized immunofluorescence-based techniques to measure mean muscle fiber cross-sectional area (CSA), fiber type-specific CSA, and fiber type distribution in the soleus and plantaris muscles (Figure 6B,F). As certain catabolic perturbations have been shown to cause muscle- and fiber type-specific changes, we chose to analyze

the soleus and plantaris muscles to assess the extent to which the effects of p21 may differ across muscles with distinct metabolic and contractile properties [17]. In line with lower levels of lean mass and muscle weight, p21OE mice display reductions in mean CSA and fiber type-specific CSA across all fiber types analyzed in both the soleus (Figure 6C,D) and plantaris (Figure 6G,H), in the absence of shifts in fiber type distribution (Figure 6E,I). As expected, there was a leftward shift in the muscle fiber CSA distribution data in p21OE mice (Fig. S2A). The total number of fibers per muscle cross section was equal between control and p21OE mice, ruling lower fiber number out as a contributing factor to reduced lean mass and muscle weight in p21OE mice (Fig. S2B).

A notable feature of senescent tissue and pathological skeletal muscle is the development of fibrosis [18–20]. To examine levels of fibrosis,

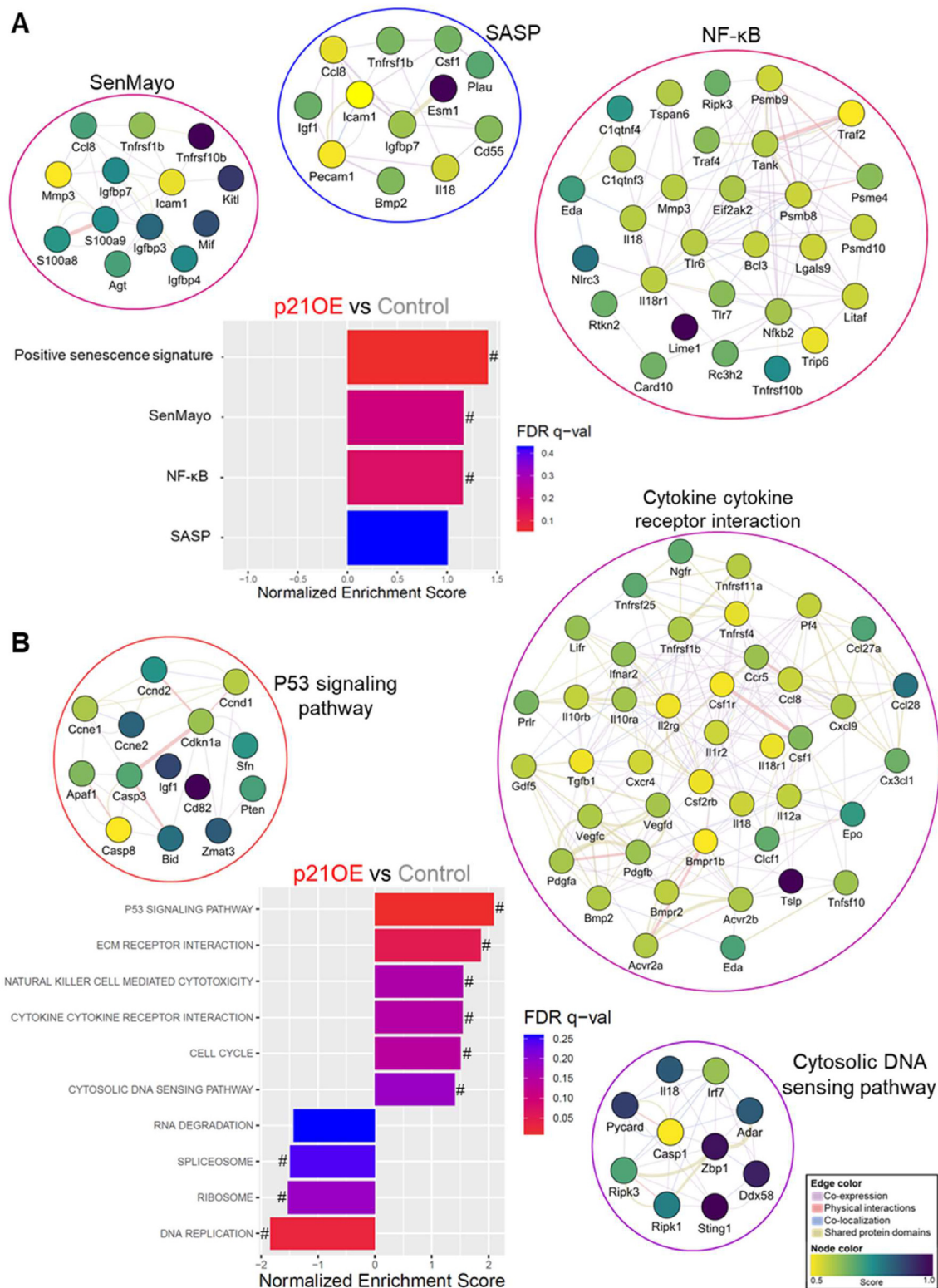


Figure 3: p21 induces a transcriptional program in skeletal muscle consistent with cellular senescence. (A-B) Enriched senescence-related pathways in p21OE mice identified by GSEA via RNA-seq of the quadriceps muscle (n = 3/group). **(A)** Curated senescence-related pathways. **(B)** KEGG pathways. Gene sets enriching SenMayo, SASP, NF-κB, p53 signaling, cytokine–cytokine receptor interaction, and cytosolic DNA sensing pathway are visualized via colored gene nodes and edges to illustrate the relationships between genes within a given pathway. The colors of gene nodes and edges are scaled to an interaction score and network category, respectively. # denotes false discovery rate (FDR) q value < 0.25.

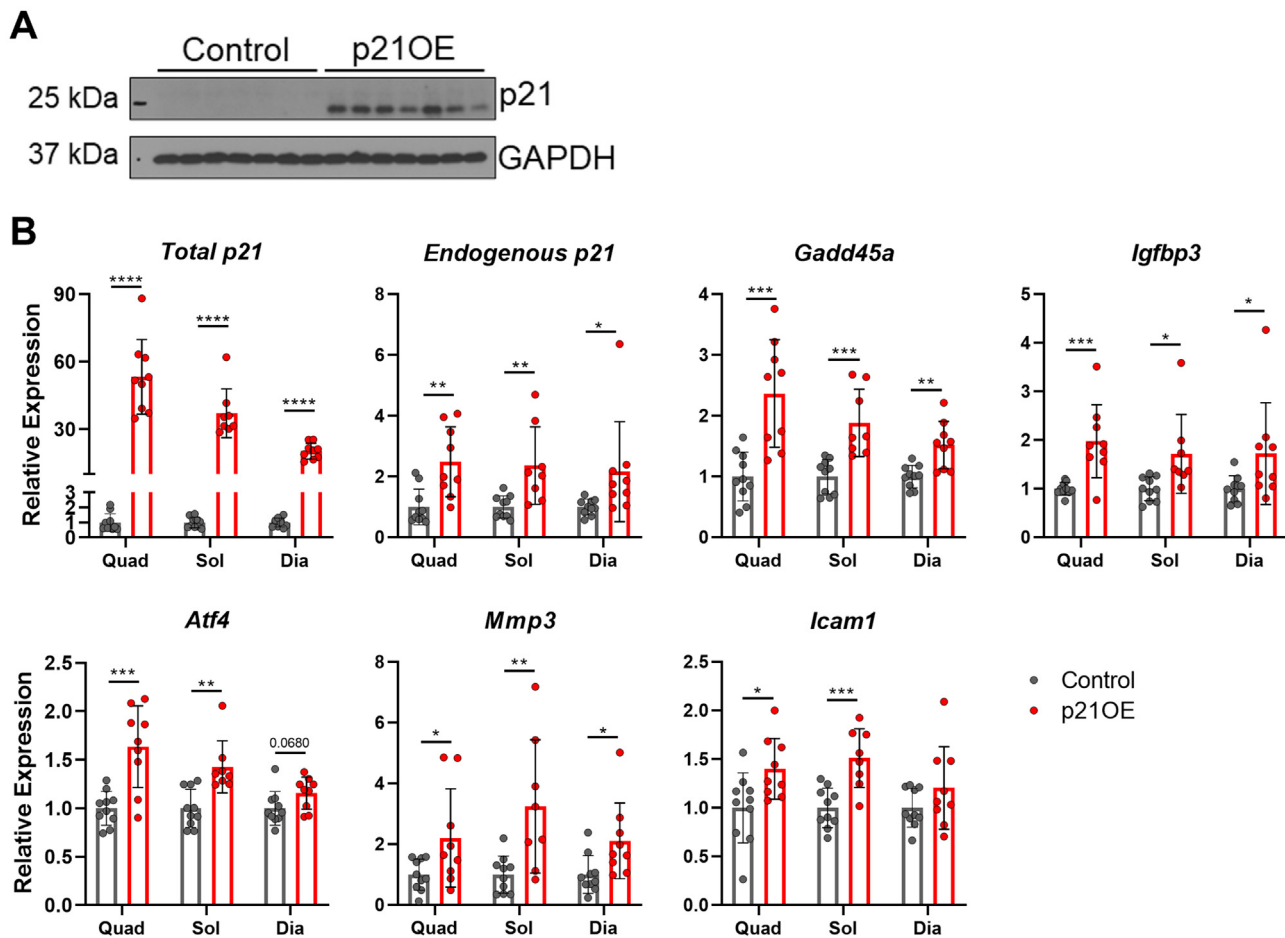


Figure 4: Accretion of p21 and increased expression of senescence markers across skeletal muscles in response to p21OE. (A) Western blot of p21 and GAPDH in quadriceps muscle ($n = 7$ /group). (B) Senescence markers in the quadriceps (Quad), soleus (Sol), and diaphragm (Dia) muscles assessed by RT-qPCR ($n = 8-10$ /group). Data represent means \pm SD. * $P < 0.05$; ** $P < 0.01$; *** $P < 0.001$, as assessed by unpaired two-tailed t tests.

we stained skeletal muscle cross sections with picrosirius red (PSR) and imaged them under brightfield and polarized light conditions (Figure 6J,K). Consistent with increased senescent cell burden, we discovered a fibrotic phenotype in skeletal muscle from p21OE mice (Figure 6L). Further, p21OE mice have a marked accumulation of densely organized collagens, a phenotype consistent with that of degenerative skeletal muscle diseases (Figure 6M) [20]. To help evaluate the translatability of these findings, we assessed clinically relevant measures of skeletal muscle health and aging. p21OE mice exhibit meaningful reductions in physical function, including treadmill performance and grip strength (Figure 6N).

Lastly, we assessed the relationship between mitochondrial function and performance on the treadmill test and provide evidence for skeletal muscle mitochondrial OCR influencing treadmill performance (Figure 6O), supporting the link between mitochondrial dysfunction and functional decline seen in humans [21].

4. DISCUSSION

While senescence plays an important role during tissue repair and as a tumor suppressor, it has become clear that the accumulation of senescent cells is also a fundamental aging mechanism that promotes tissue dysfunction and ultimately disease [22–24]. Work from our

group, and others, suggests that senescent cells may contribute to deficits in skeletal muscle function and health [25–29]. Most recently, we identified p21 as a distinguishing feature of cellular senescence and functional decline in skeletal muscle [7]. Herein, we used a novel p21OE mouse to determine the extent to which p21 directly contributes to cellular senescence and skeletal muscle dysfunction. We found that p21 induces a transcriptional program remarkably consistent with the senescence program, enriched in DNA damage response, cell-cycle arrest, and inflammatory signaling pathways. Further molecular analysis revealed distinct phenotypes of cellular senescence to be present in p21OE mice, including mitochondrial dysfunction, DNA damage, and a robust SASP. We also show that p21 drives key aspects of skeletal muscle pathology, including tissue fibrosis, low levels of skeletal muscle mass, and reductions in physical function. Exercise, a well-recognized function-promoting therapy, has been shown to reduce senescence markers in skeletal muscle and circulation [30–32]. Elucidating the interplay between exercise-induced reductions in senescent cell burden and improvements in skeletal muscle health is an exciting area of future study.

A limitation to this study is the ubiquitous and constitutive nature of p21 expression in our mouse model. Models that allow for greater temporal and spatial control of p21 are necessary to assess age- and tissue-specific responses to p21.

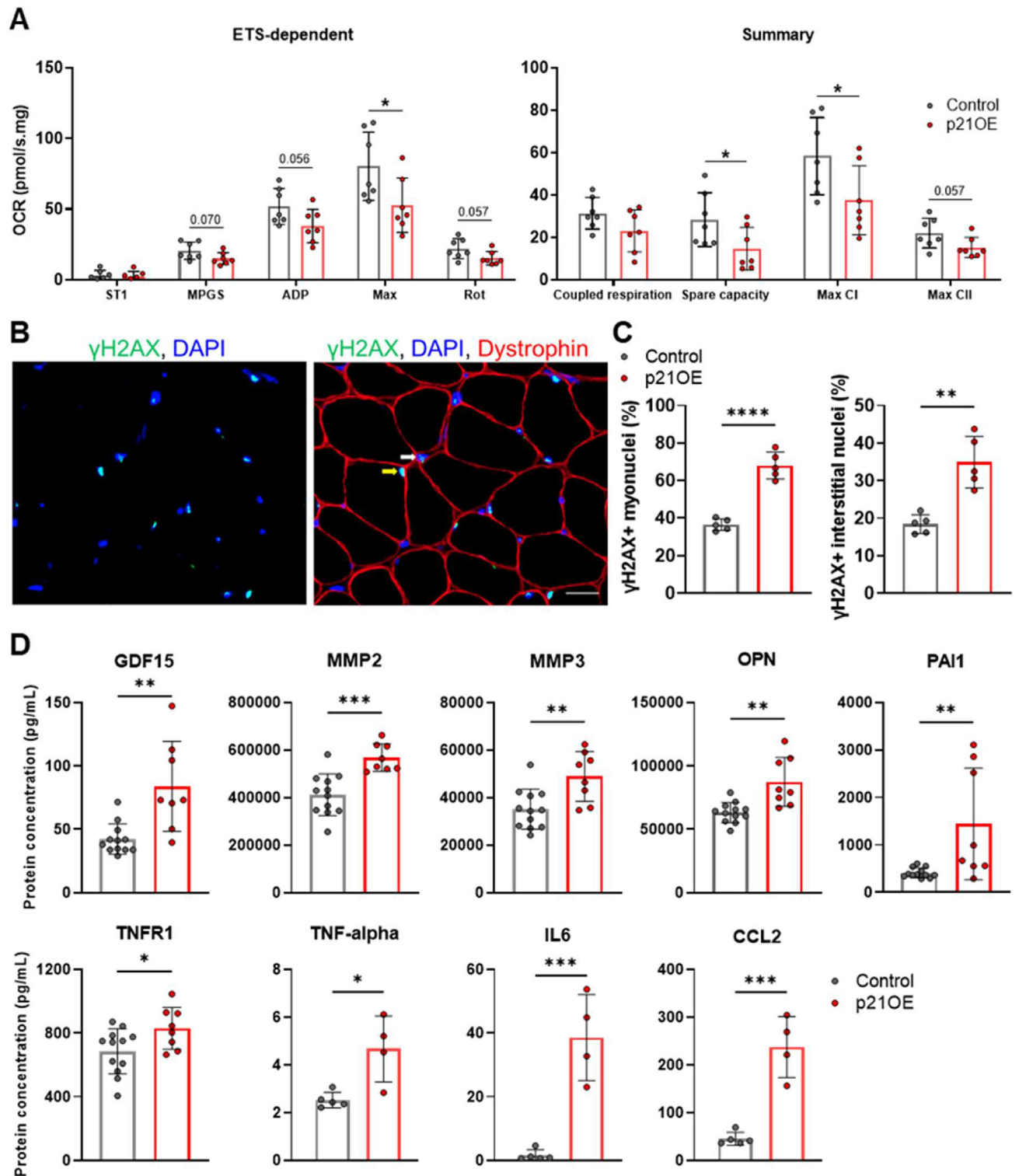


Figure 5: p21 gives rise to hallmarks of cellular senescence. (A) Oxygen consumption rates (OCR) in muscle fiber mitochondria measured using high-resolution respirometry (n = 7/group). OCR, oxygen consumption rates; ST1, respiratory state 1; MPGS, malate, pyruvate, glutamate, succinate; ADP, respiration in presence of MPGS plus ADP; Max, maximal respiration (after FCCP titration); Rot, respiration after rotenone (complex I inhibitor) addition. (B) Representative immunofluorescence images of soleus muscle cross sections stained for γ H2AX, DAPI, and dystrophin. Nuclei inside the dystrophin border were classified as myonuclei (yellow arrow) and those outside the fiber border were classified as interstitial nuclei (white arrow). (C) Quantification of the percentage of γ H2AX + myonuclei and γ H2AX + interstitial nuclei (n = 5/group). (D) Protein concentrations of circulating SASP factors measured with Magpix (n = 8–12/group) and ELLA (4–5/group) multiplexing platforms. Scale bar, 20 μ m. Data represent means \pm SD. * P < 0.05; ** P < 0.01; *** P < 0.001, **** P < 0.0001, as assessed by unpaired two-tailed t tests.

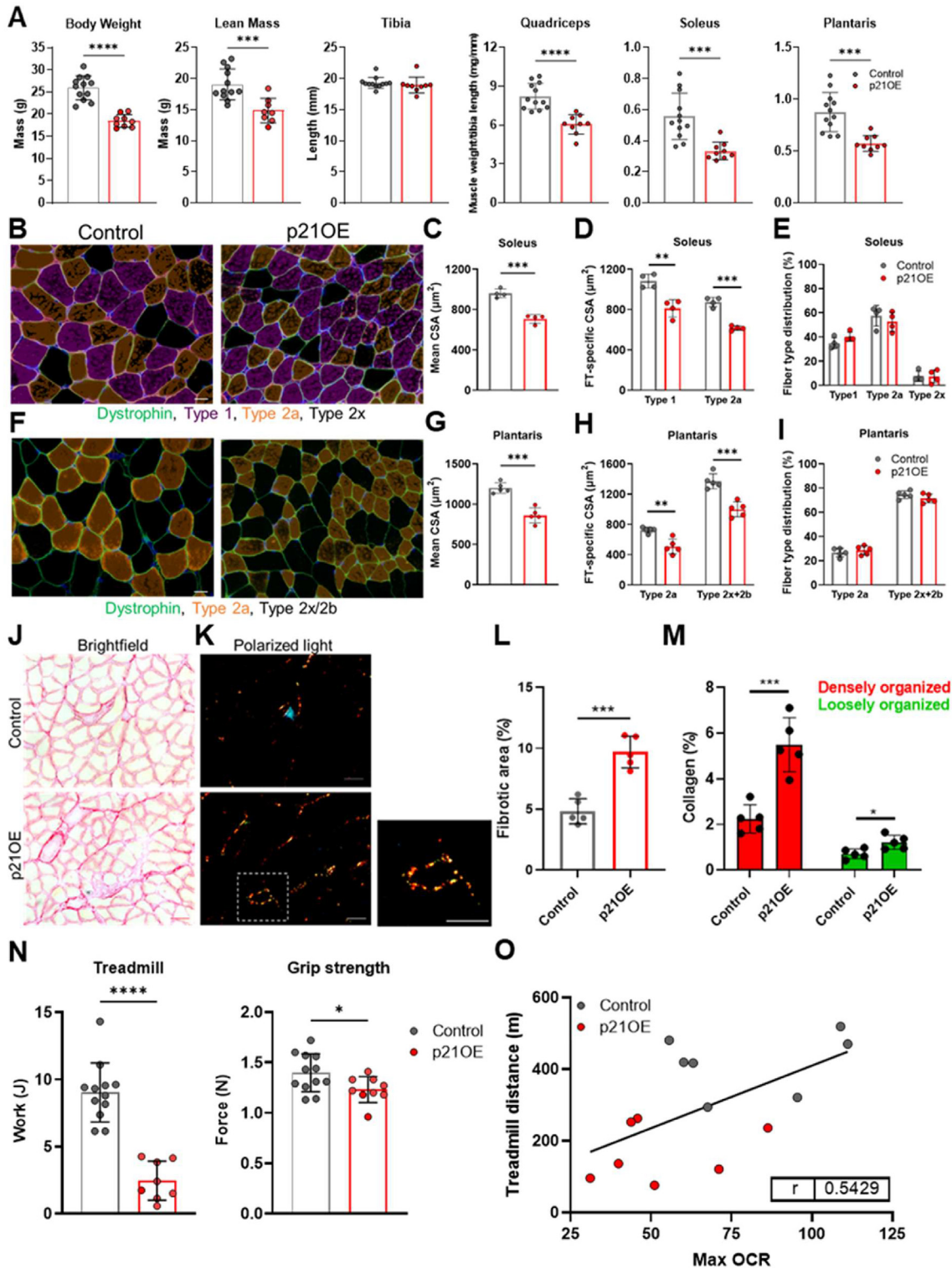


Figure 6: p21 drives skeletal muscle pathophysiology. (A) Body weight, lean mass, tibia length, and skeletal muscle weights in control and p21OE mice ($n = 9\text{--}12/\text{group}$). (B) Representative immunofluorescence images of soleus muscle cross sections stained for dystrophin, myosin heavy chain 1 (Type 1), and myosin heavy chain 2a (Type 2a). (C–E) Quantification of mean cross-sectional area (CSA), fiber type-specific CSA, and fiber type distribution in the soleus ($n = 4/\text{group}$). (F) Representative immunofluorescence images of plantaris muscle cross sections stained for dystrophin and myosin heavy chain 2a (Type 2a). (G–I) Quantification of mean CSA, fiber type-specific CSA, and fiber type distribution in the plantaris ($n = 5/\text{group}$). (J–K) Representative PSR-stained soleus muscle cross sections visualized with brightfield and polarized light microscopy. (L–M) Relative area positive for PSR and red and green emitted light ($n = 5/\text{group}$). (N) Treadmill and grip strength tests ($n = 8\text{--}12/\text{group}$). (O) Association between max oxygen consumption rate (OCR) in muscle fiber mitochondria and distance traveled in the treadmill test ($n = 14$; $P = 0.0479$). Scale bars, 20 μm for B and F and 50 μm for J and K. Data represent means \pm SD. * $P < 0.05$; ** $P < 0.01$; *** $P < 0.001$, **** $P < 0.0001$, as assessed by unpaired two-tailed t tests.

Taken together, our findings identify p21 as a powerful signaling molecule in skeletal muscle that induces cellular senescence and propagates tissue dysfunction. These results suggest senescent cells may represent a druggable target in skeletal muscle. In order to determine the feasibility of targeting cellular senescence to restore skeletal muscle health and function, gain- and loss-of-function models that enable the modulation of p21 in a skeletal muscle-specific fashion are necessary.

AUTHOR CONTRIBUTIONS

D.A.E designed and oversaw all experiments. D.A.E, A.J, Z.A, X.Z, I.S, A.E.S, J.D.Z, G.M.W, C.M and T.A.W planned and performed experiments and interpreted results. E.N.C, D.J.B, J.M.v.D, and N.K.L provided guidance throughout. D.A.E wrote the manuscript. All authors reviewed the manuscript.

DATA AVAILABILITY

Data will be made available on request.

ACKNOWLEDGMENTS

This work was supported by NIH NATIONAL INSTITUTE ON AGING grants to N.K.L (AG060907, AG062413, and AG055529) and D.A.E and I.S (T32AG049672), the Glenn Foundation for Medical Research (N.K.L, E.N.C, and D.J.B) and the Pritzker Foundation (N.K.L).

CONFLICT OF INTEREST

D.J.B. and N.K.L are co-inventors on patent applications licensed to or filed by Unity Biotechnology, a company developing senolytic strategies for treatment of age-related disorders, including small molecules that selectively eliminate senescent cells. Research in the Baker and LeBrasseur laboratories have been reviewed by the Mayo Clinic Conflict of Interest Review Board and is being conducted in compliance with Mayo Clinic Conflict of Interest policies. J.M.v.D. is a co-founder of and holds equity in Unity Biotechnology and Cavalry Biosciences.

APPENDIX A. SUPPLEMENTARY DATA

Supplementary data to this article can be found online at <https://doi.org/10.1016/j.molmet.2022.101652>.

REFERENCES

- [1] Baker DJ, Childs BG, Durik M, Wijers ME, Sieben CJ, Zhong J, et al. Naturally occurring p16(Ink4a)-positive cells shorten healthy lifespan. *Nature* 2016;530(7589):184–9.
- [2] Childs BG, Baker DJ, Wijshake T, Conover CA, Campisi J, Deursen JMv. Senescent intimal foam cells are deleterious at all stages of atherosclerosis. *Science* 2016;354(6311):472–7.
- [3] Farr JN, Fraser DG, Wang H, Jaehn K, Ogrodnik MB, Weivoda MM, et al. Identification of senescent cells in the bone microenvironment. *Journal of Bone and Mineral Research* 2016;31(11):1920–9.
- [4] Lewis-McDougall FC, Ruchaya PJ, Domenjo-Vila E, Shin Teoh T, Prata L, Cottle BJ, et al. Aged-senescent cells contribute to impaired heart regeneration. *Aging Cell* 2019;18(3):e12931.
- [5] Coppé JP, Patil CK, Rodier F, Sun Y, Muñoz DP, Goldstein J, et al. Senescence-associated secretory phenotypes reveal cell-nonautonomous functions of oncogenic RAS and the p53 tumor suppressor. *PLoS Biol* 2008;6(12):2853–68.
- [6] Schafer MJ, Zhang X, Kumar A, Atkinson EJ, Zhu Y, Jachim S, et al. The senescence-associated secretome as an indicator of age and medical risk. *JCI Insight* 2020;5(12).
- [7] Zhang X, Habiballa L, Aversa Z, Ng YE, Sakamoto AE, Englund DA, et al. Characterization of cellular senescence in aging skeletal muscle. *Nature Aging* 2022;2: 601–15.
- [8] Avelar RA, Ortega JG, Tacutu R, Tyler EJ, Bennett D, Binetti P, et al. A multidimensional systems biology analysis of cellular senescence in aging and disease. *Genome Biol* 2020;21(1):91.
- [9] Saul D, Kosinsky RL, Atkinson EJ, Doolittle ML, Zhang X, LeBrasseur NK, et al. A new gene set identifies senescent cells and predicts senescence-associated pathways across tissues. *Nature Communications* 2022;13(1):4827.
- [10] Passos JF, Nelson G, Wang C, Richter T, Simillion C, Proctor CJ, et al. Feedback between p21 and reactive oxygen production is necessary for cell senescence. *Mol Syst Biol* 2010;6:347.
- [11] Short KR, Bigelow ML, Kahl J, Singh R, Coenen-Schimke J, Raghavakaimal S, et al. Decline in skeletal muscle mitochondrial function with aging in humans. *Proc Natl Acad Sci U S A* 2005;102(15):5618–23.
- [12] Stefanatos R, Sanz A. Mitochondrial complex I: a central regulator of the aging process. *Cell Cycle* 2011;10(10):1528–32.
- [13] Jurk D, Wang C, Miwa S, Maddick M, Korolchuk V, Tzolou A, et al. Postmitotic neurons develop a p21-dependent senescence-like phenotype driven by a DNA damage response. *Aging Cell* 2012;11(6):996–1004.
- [14] Yousefzadeh M, Henpita C, Vyas R, Soto-Palma C, Robbins P, Niedernhofer L. DNA damage-how and why we age? *Elife* 2021;10.
- [15] Martini H, Passos JF. Cellular senescence: all roads lead to mitochondria. *FEBS J* 2022. <https://doi.org/10.1111/febs.16361>.
- [16] Sturmlechner I, Zhang C, Sine CC, van Deursen EJ, Jeganathan KB, Hamada N, et al. p21 produces a bioactive secretome that places stressed cells under immunosurveillance. *Science* 2021;374(6567):eabb3420.
- [17] Bass JJ, Hardy EJO, Inns TB, Wilkinson DJ, Piasecki M, Morris RH, et al. Atrophy resistant vs. Atrophy susceptible skeletal muscles: "aRaS" as a novel experimental paradigm to study the mechanisms of human disuse atrophy. *Front Physiol* 2021;12:653060.
- [18] Schafer MJ, White TA, Iijima K, Haak AJ, Ligresti G, Atkinson EJ, et al. Cellular senescence mediates fibrotic pulmonary disease. *Nat Commun* 2017;8:14532.
- [19] Fry CS, Lee JD, Mula J, Kirby TJ, Jackson JR, Liu F, et al. Inducible depletion of satellite cells in adult, sedentary mice impairs muscle regenerative capacity without affecting sarcopenia. *Nature medicine* 2015;21(1):76.
- [20] Petrosino JM, Leask A, Accornero F. Genetic manipulation of CCN2/CTGF unveils cell-specific ECM-remodeling effects in injured skeletal muscle. *Faseb J* 2019;33(2):2047–57.
- [21] Romanello V, Sandri M. The connection between the dynamic remodeling of the mitochondrial network and the regulation of muscle mass. *Cell Mol Life Sci* 2021;78(4):1305–28.
- [22] Demaria M, Ohtani N, Youssef SA, Rodier F, Toussaint W, Mitchell JR, et al. An essential role for senescent cells in optimal wound healing through secretion of PDGF-AA. *Dev Cell* 2014;31(6):722–33.
- [23] van Deursen JM. The role of senescent cells in ageing. *Nature* 2014;509(7501):439–46.
- [24] Young LV, Wakelin G, Cameron AWR, Springer SA, Ross JP, Wolters G, et al. Muscle injury induces a transient senescence-like state that is required for myofiber growth during muscle regeneration. *Faseb J* 2022;36(11):e22587.
- [25] da Silva PFL, Ogrodnik M, Kucheryavenko O, Glibert J, Miwa S, Cameron K, et al. The bystander effect contributes to the accumulation of senescent cells in vivo. *Aging Cell* 2019;18(1).
- [26] Dungan CM, Murach KA, Zdunek CJ, Tang ZJ, VonLemden GL, Brightwell CR, et al. Deletion of SA β -Gal+ cells using senolytics improves muscle regeneration in old mice. *Aging Cell* 2021:e13528.

- [27] Englund DA, Zhang X, Aversa Z, LeBrasseur NK. Skeletal muscle aging, cellular senescence, and senotherapeutics: current knowledge and future directions. *Mech Ageing Dev* 2021;200:111595.
- [28] Baker DJ, Jeganathan KB, Cameron JD, Thompson M, Juneja S, Kopecka A, et al. BubR1 insufficiency causes early onset of aging-associated phenotypes and infertility in mice. *Nat Genet* 2004;36(7):744–9.
- [29] Sousa-Victor P, Gutarra S, García-Prat L, Rodríguez-Ubrea J, Ortet L, Ruiz-Bonilla V, et al. Geriatric muscle stem cells switch reversible quiescence into senescence. *Nature* 2014;506(7488):316–21.
- [30] Bechshøft CJL, Jensen SM, Schjerling P, Andersen JL, Svensson RB, Eriksen CS, et al. Age and prior exercise in vivo determine the subsequent in vitro molecular profile of myoblasts and nonmyogenic cells derived from human skeletal muscle. *Am J Physiol Cell Physiol* 2019;316(6):C898–c912.
- [31] Englund DA, Sakamoto AE, Fritsche CM, Heeren AA, Zhang X, Kotajarvi BR, et al. Exercise reduces circulating biomarkers of cellular senescence in humans. *Aging Cell* 2021:e13415.
- [32] Zhang X, Englund DA, Aversa Z, Jachim SK, White TA, LeBrasseur NK. Exercise counters the age-related accumulation of senescent cells. *Exerc Sport Sci Rev* 2022;50(4):213–21.
- [33] Madisen L, Zwingman TA, Sunkin SM, Oh SW, Zariwala HA, Gu H, et al. A robust and high-throughput Cre reporting and characterization system for the whole mouse brain. *Nat Neurosci* 2010;13(1):133–40.
- [34] Viggars MR, Wen Y, Peterson CA, Jarvis JC. Automated cross-sectional analysis of trained, severely atrophied, and recovering rat skeletal muscles using MyoVision 2.0. *J Appl Physiol* 2022;132(3):593–610. 1985.
- [35] Englund DA, Figueiredo VC, Dungan CM, Murach KA, Peck BD, Petrosino JM, et al. Satellite cell depletion disrupts transcriptional coordination and muscle adaptation to exercise. *Function* 2020;2(1).
- [36] Subramanian A, Tamayo P, Mootha VK, Mukherjee S, Ebert BL, Gillette MA, et al. Gene set enrichment analysis: a knowledge-based approach for interpreting genome-wide expression profiles. *Proc Natl Acad Sci U S A* 2005;102(43):15545–50.
- [37] Warde-Farley D, Donaldson SL, Comes O, Zuberi K, Badrawi R, Chao P, et al. The GeneMANIA prediction server: biological network integration for gene prioritization and predicting gene function. *Nucleic Acids Res* 2010;38(Web Server issue):W214–20.
- [38] Schafer MJ, White TA, Evans G, Tonne JM, Verzosa GC, Stout MB, et al. Exercise prevents diet-induced cellular senescence in adipose tissue. *Diabetes* 2016;65(6):1606–15.
- [39] LeBrasseur NK, Schelhorn TM, Bernardo BL, Cosgrove PG, Loria PM, Brown TA. Myostatin inhibition enhances the effects of exercise on performance and metabolic outcomes in aged mice. *J Gerontol A Biol Sci Med Sci* 2009;64(9):940–8.